Acta Polytechnica CTU Proceedings **55**:16–24, 2025
https://doi.org/10.14311/APP.2025.55.0016

Published by the Czech Technical University in Prague

HIGH-TEMPERATURE OXIDATION OF NON-ZIRCONIUM MATERIALS FOR ATF

Alžběta Endrychová[a,c,*], Jakub Krejčí[c], Martin Ševeček[b,c], Martin Cesnek[b], Claudia Aparicio[d], David Rada[c]

[a] *Czech Technical University in Prague, Faculty of Mechanical Engineering, Department of Energy Engineering, Technická 4, 166 07 Prague 6, Czech Republic*

[b] *Czech Technical University in Prague, Faculty of Nuclear Sciences and Physical Engineering, Department of Nuclear Reactors, V Holešovičkách 2, 180 00 Prague 8, Czech Republic*

[c] *UJP PRAHA a.s., Nad Kamínkou 1345, 156 00 Prague – Zbraslav, Czech Republic*

[d] *Research Centre Řež, Hlavni 130, 250 68 Husinec – Řež, Czech Republic*

[*] corresponding author: alzbeta.endrychova@fs.cvut.cz

Abstract. Non-zirconium materials, such as silicon carbide (SiC) and FeCrAl alloys, have attracted interest for developing Accident-Tolerant Fuel (ATF) cladding systems owing to their superior high-temperature oxidation resistance. SiC offers excellent thermal stability, high-temperature properties, irradiation tolerance, and low activation, while FeCrAl alloys provide outstanding oxidation resistance in steam and air through a stable alumina (Al_2O_3) layer. This study examines their oxidation behavior under simulated severe-accident conditions. Microstructural changes and mechanical integrity after exposure were analyzed using scanning electron microscopy (SEM) and ring compression tests (RCT). The analysis revealed material-specific strengths and limitations, emphasizing the role of temperature and oxidation environment.

Keywords: Oxidation, Accident-Tolerant Fuel (ATF), Silicon-Carbide (SiC), FeCrAl.

1. Introduction

Accident-Tolerant Fuel (ATF) cladding concepts aim to reduce the rate and total amount of hydrogen and heat generated by high-temperature oxidation in Light-Water Reactor (LWR) severe accidents. Protective oxide scales based on chromia, alumina, or silica can significantly suppress oxidation kinetics [1]. Figure 1 compares the parabolic rate constants for candidate cladding materials in steam with those of conventional Zr-4.

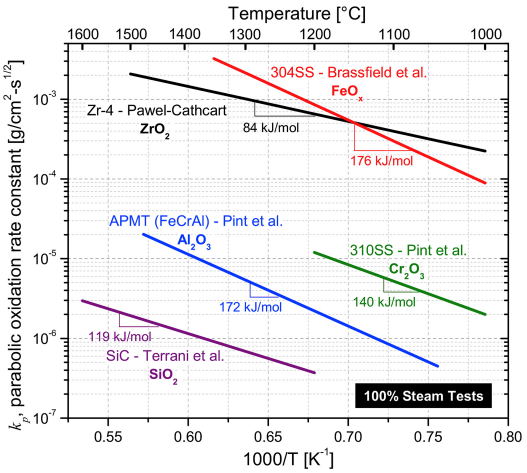

Figure 1. Parabolic oxidation rate constants for various cladding materials and their resulting oxides in steam as a function of temperature [2].

This study evaluated two non-zirconium candidates: a triplex SiC/SiC composite cladding (SiC-CTP) and a ferritic FeCrAl alloy (B136Y3). High-temperature oxidation (HTO) in steam was examined up to 1 550 °C for SiC-CTP and up to 1 375 °C for FeCrAl. Microstructure was analyzed using SEM, X-ray diffraction (XRD), and Mössbauer spectroscopy, while mechanical integrity was assessed by the ring compression test (RCT).

2. Materials and experimental methods

2.1. SiC/SiC composite cladding

SiC fibers are widely used in composites exposed to high-temperature oxidizing environments. Ceramic matrix composites (CMC) reinforced with SiC fibers exhibit high toughness, excellent mechanical properties, and good resistance to thermal shock [3]. Thus, SiC CMC are strong candidates for ATF cladding in LWRs, with the potential for the highest survival temperature during severe-accident scenarios.

In a water vapor environment, the oxidation of SiC proceeds as in Reaction 1, while volatilization of SiO_2 occurs according to Reaction 2 [3, 4]:

$$\mathrm{SiC\ (s) + 3H_2O\ (g) \rightarrow SiO_2\ (s) + 3H_2\ (g) + CO\ (g)}, \quad (1)$$

$$\mathrm{SiO_2\ (s) + 2H_2O\ (g) \rightarrow Si(OH)_4\ (g)}, \quad (2)$$

$$SiO_2\ (s) + H_2O\ (g) \rightarrow Si(OH)_2\ (g). \qquad (3)$$

During high-temperature oxidation, a protective silicon oxide layer is formed according to Reaction 1. Hydrogen is released in addition to carbon-containing gases. At higher temperatures, volatile hydroxides or oxyhydroxides may form (Reactions 2 and 3). Furthermore, silicon monoxide (SiO) may form at low oxygen partial pressures and elevated temperatures.

Steinbrück et al. [4] performed a series of steam oxidation experiments on SiC/SiC composite cladding up to 1 845 °C. Although a transient test at approximately 1 845 °C caused localized failure by consuming the external CVD-SiC layer, two isothermal tests at 1 700 °C for one hour showed no macroscopic damage or significant oxidation. The SiC seal-coat effectively protected the fiber–matrix structure, keeping gas release rates low and mechanical degradation minimal.

Despite its outstanding oxidation resistance and mechanical performance, SiC composite cladding in LWRs faces several challenges. Reliable assessment requires the fabrication of tubes with tightly controlled and reproducible properties. In addition, the development of robust joining techniques for end plugs [5] and the mitigation of matrix microcracking remain major technical obstacles [6, 7].

The SiC samples used in this study were provided by CTP USA. The microstructure of the as-received triplex SiC cladding (SiC-CTP) is shown in Figure 2. It consists of a monolithic SiC inner layer, a SiC/SiC composite intermediate layer, and a monolithic SiC outer layer. The SiC inner layer primarily prevents radioactive fission products from escaping into the coolant, the composite layer enhances strength and fracture toughness, and the outer layer protects against corrosive coolant water at high temperatures.

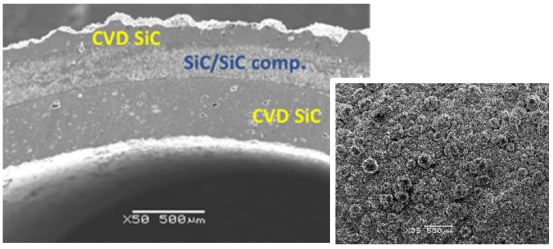

FIGURE 2. Microstructure of SiC-CTP sample in as-received state: cut (left) and surface (right).

2.2. FeCrAl (B136Y3)

Fe-based alloys such as FeCrAl combine superior oxidation resistance with good mechanical properties compared to traditional Zr alloys [2]. Both oxide dispersion-strengthened (ODS) alloys with reduced Cr content [8] and conventional non-ODS nuclear-grade FeCrAl alloys were developed as ATF concepts. Compared to commercial Kanthal, nuclear-grade FeCrAl alloys contain less Cr to mitigate formation of the embrittling Cr-rich α' phase under irradiation at intermediate temperatures [9].

Figure 3 shows the parabolic oxidation rate constants of the nuclear-grade FeCrAl alloys B136Y3 and C26M2, based on the measurements reported by Kim et al. [10], compared with literature data for alumina and iron oxide formation. At temperatures above 1 200 °C, the alloys exhibited a significant increase in oxidation kinetics, closely approaching those of Fe oxides. This behavior indicates a breakdown of the protective alumina scale and the onset of rapid, non-protective oxidation.

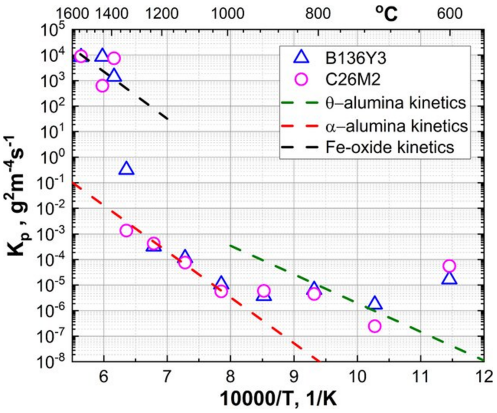

FIGURE 3. Parabolic rate constants of B136Y3 and C26M2 as a function of temperature, compared with Fe oxides, α-alumina, and θ-alumina [10].

A limitation is that the higher neutron absorption cross-section of Fe and Cr requires thinner cladding wall thicknesses. The ferritic FeCrAl (B136Y3) samples used in this study were provided by the QUENCH-19 experiment conducted at KIT. The alloy is highly resistant to corrosion owing to the formation of a protective alumina layer. Its chemical composition and manufacturing process are described in detail elsewhere [10, 11]. The microstructure of the as-received sample is shown in Figure 4.

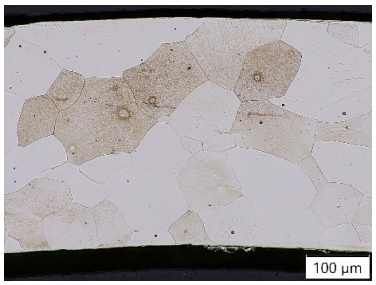

FIGURE 4. Microstructure of FeCrAl (B136Y3) sample in as-received state.

2.3. Experimental methods

The high-temperature oxidation experiments were performed in an electric resistance furnace under an argon–steam atmosphere (Figure 5). Both surfaces of the samples were exposed to the oxidizing atmosphere.

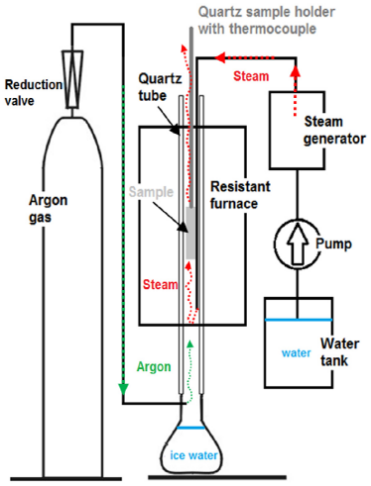

Figure 5. Schematic of the high-temperature oxidation experiment.

The temperature was measured in the middle of each sample using a B-type thermocouple. After exposure, specimens were directly quenched in a water–ice mixture. For comparison, tests were also carried out with successive cooling in air without quenching. Experiments were performed on specimens of length 25 mm at temperatures from 1 100 °to 1 550 °C for different times for SiC-CTP samples (Table 1) and from 1 300 °C up to 1 375 °C for FeCrAl samples (Table 2).

For zirconium alloys, the limiting temperature is generally set at 1 204 °C, which corresponds to 17 % Equivalent Cladding Reacted (ECR) according to the Cathcart–Pawel (CP) correlation for exposure times around 5 minutes. In comparison with the ECR-CP values for zirconium alloys, the test conditions for the investigated samples were several times more severe.

The samples were weighed before and after exposure using a Mettler Toledo XS 105 analytical balance with a resolution of 0.01 mg to determine the weight gain. After oxidation, the samples were cut using a diamond saw for subsequent analyses.

The microstructure of the samples was examined using an optical microscope Nikon EPIPHOT 300 and a scanning electron microscope (SEM) JEOL JSM-5510LV. The thickness of the layers was measured at four locations along the sample perimeter.

Surface XRD analysis was performed using a third-generation Empyrean diffractometer with a cobalt source, at an incidence angle of 10–70°. The maximum penetration depth of the X-ray radiation was approximately 200 µm.

Transmission Mössbauer spectra (TMS) were recorded at room temperature (RT) using a constant-acceleration spectrometer equipped with a ^{57}Co(Rh) source. Oxidized fragments of the samples were ground into fine powder, and the spectra were acquired in transmission geometry. To investigate the near-surface region with an information depth of approximately 100 nm, Conversion Electron Mössbauer Spectroscopy (CEMS) was employed. All isomer shifts (IS) are reported relative to a bcc-Fe reference foil measured at RT. Mössbauer spectral parameters – including isomer shift (IS), quadrupole splitting/shift (QS), hyperfine magnetic field (B_{hf}), and component areas (A), as well as the relative line intensities of magnetic sextets – were determined using the CONFIT curve-fitting software [12].

Microhardness was measured using a Buehler MICROMET 5114 (Vickers hardness test, ASTM E384). Since neither the microhardness of the outer layer of SiC-CTP nor of the composite layer could be measured, the test was carried out on the inner monolithic

Temperature [°C]	Time [min]	ECR-CP [%]
1 100	30	14.4
1 200	5	10.3
1 200	15	16.0
1 200	30	23.3
1 200	60	32.7
1 200*	60	32.7
1 200*	30	23.3
1 200*	30	23.3
1 300	30	36.2
1 350	30	40.7
1 400	15	37.8
1 400	30	73.8
1 400	60	53.4
1 450	1	14.5
1 450	30	63.0
1 500	5	32.8
1 550	5	36.9

* samples without quenching

Table 1. Experimental matrix of SiC-CTP samples compared to ECR-CP (Cathcart–Pawel Equivalent Cladding Reacted) for zirconium alloys.

Temperature [°C]	Time [min]	ECR-CP [%]
1 300	180	248
1 300	90	176
1 300	30	102
1 350	180	302
1 350	60	179
1 350	30	125
1 350	120	248
1 350	90	214
1 360	5	55
1 375 (RAMP)	6.5	–
1 375	5	59
1 375	30	137

Table 2. Experimental matrix of FeCrAl samples compared to ECR-CP (Cathcart–Pawel Equivalent Cladding Reacted) for zirconium alloys.
Note: RAMP = gradual heating from 900 to 1 375 °C (6.5 min total).

SiC layer. Ten indents were performed (HV1 for SiC-CTP samples and HV0.1 for FeCrAl samples) in the middle of the inner layer.

Mechanical tests were performed using RCT on an INSTRON 1185 R5800 at 135 °C. The loading speed was kept constant at 1 mm min^{-1}.

3. Results

3.1. High-temperature oxidation

Figure 6 presents the time dependence of weight gain for SiC-CTP in comparison with FeCrAl. For SiC-based specimens, the net mass change resulted from two competing processes: (1) volatilization of surface oxides leading to mass loss, and (2) oxidation of the substrate leading to mass gain. The measurement therefore reflected only the cumulative effect of these processes, while their individual contributions – potentially varying with layer thickness – could not be resolved. At shorter exposure times volatilization dominated, whereas at longer durations oxidation became prevalent.

For the SiC-CTP samples, changes in weight gain or oxide thickness were negligible (on the order of micrometers). In contrast, FeCrAl samples exposed to temperatures above 1 300 °C exhibited markedly reduced or even negative weight gains, indicating oxide spallation. Under such conditions, oxidation kinetics could not be reliably assessed without continuous mass monitoring, even when accounting for detached fine powder.

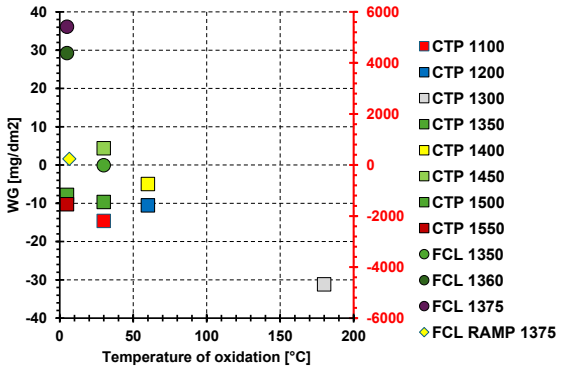

Figure 6. Weight gain (WG) as a function of oxidation temperature for SiC-CTP and FeCrAl (FCL) samples.

Figures 7 and 8 show macroscopic images and microstructures of SiC-CTP after high-temperature oxidation at 1 200 °C and 1 550 °C. In Figure 7a, a significant non-uniformity of the individual layers was observed. After 15 min (Figure 7b) and 30 min (Figure 7c) at 1 200°C, the color of the samples changed to purple and green. The dependence of thickness growth for samples oxidized at 1 200 °C is shown in Figure 9. From the images and subsequent measurements, it was evident that the layers were not uniform

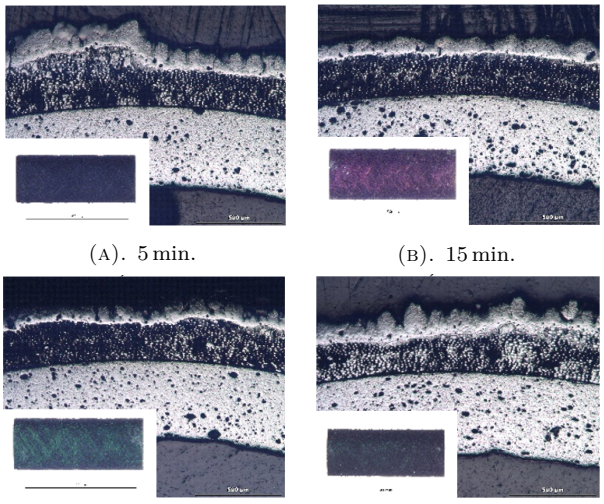

(a). 5 min. (b). 15 min.

(c). 30 min. (d). 60 min.

Figure 7. Microstructure of SiC-CTP after high-temperature oxidation at 1 200 °C for different exposure times.

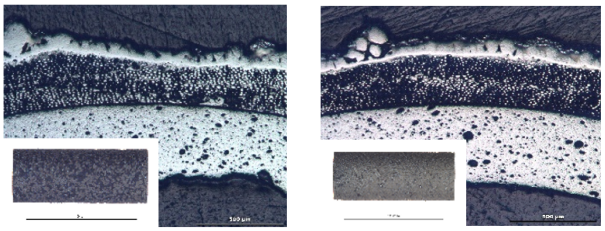

(a). At 1 500 °C. (b). At 1 550 °C.

Figure 8. Microstructure of SiC-CTP after high-temperature oxidation for 5 min.

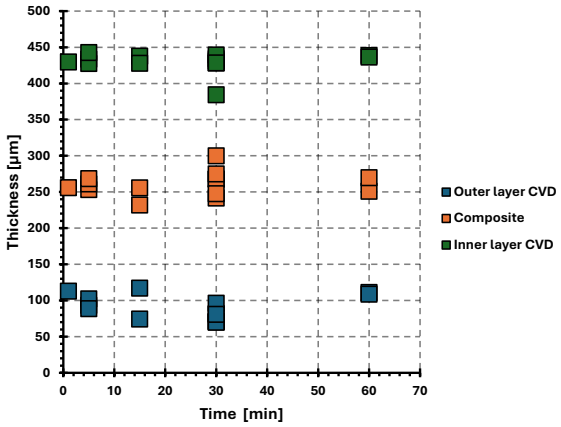

Figure 9. Dependence of thickness growth of outer, inner CVD layer, and SiC/SiC composite thickness with time for samples oxidized at 1 200 °C.

and that the dissolution rate could not be reliably determined.

The FeCrAl samples were tested at 1 300 °C to 1 375 °C. Images of the samples after the tests are shown in Figure 10. Samples oxidized between 1 300 °C and 1 350 °C showed no visible changes compared to the as-received state (Figure 10a). After

5 min at 1 360 °C (Figure 10b), the sample completely oxidized, turned black, and began to disintegrate. After 30 min at 1 375 °C (Figure 10c), only fragments of the disintegrated sample remained. Above 1 360 °C, iron oxides with fast growth kinetics formed, leading to rapid degradation. By contrast, the RAMP test (gradual heating from 900 °C to 1 375 °C, total exposure time 6.5 min) produced an intact sample (Figure 10d), indicating that sufficient time had been available for the formation of a protective alumina (Al_2O_3) layer.

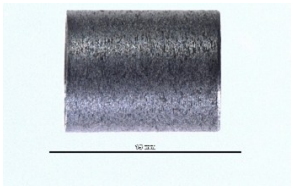

(A). 1 350 °C, 30 min.

(B). 1 360 °C, 5 min.

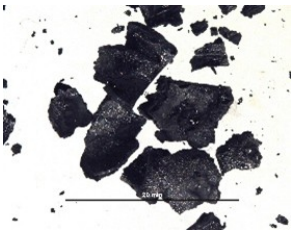

(C). 1 375 °C, 30 min.

(D). RAMP test to 1 375 °C, total 6.5 min.

Figure 10. FeCrAl after high-temperature oxidation.

3.2. Microstructure analysis

Figure 11 shows SEM images of SiC-CTP: (a) in the as-received state and (b) after oxidation at 1 400 °C for 30 min. After exposure, crystals of SiO_2 were observed on the surface.

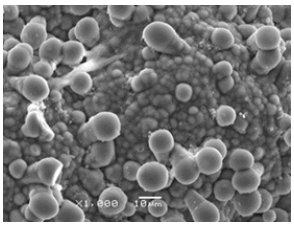

(A).

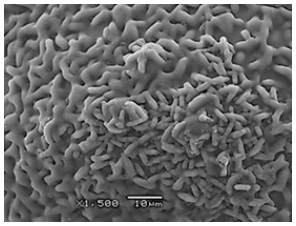

(B).

Figure 11. SEM images of SiC-CTP: (a) as-received state, (b) after high-temperature steam oxidation for 30 min at 1 400 °C.

XRD analysis confirmed these changes. Proportional representation of phases from surface XRD measurement is shown in Table 3. In the as-received state (Figure 12), the phases included elemental silicon, cubic (3C-SiC) and hexagonal (6H-SiC) SiC, and SiO_2 in the form of coesite. After oxidation at 1 550 °C for 5 min (Figure 13), cristobalite was detected instead of coesite, while Si and SiC remained.

Phase	As-received	1 550 °C/5 min
Si	76.9 wt. %	71.0 wt. %
SiC-3C	14.2 wt. %	26.9 wt. %
SiC-6H	5.2 wt. %	–
SiO_2 (cristobalite)	–	2.1 wt. %
SiO_2 (coesite)	3.7 wt. %	–

Table 3. Proportional representation of phases from surface XRD measurements of SiC-CTP.

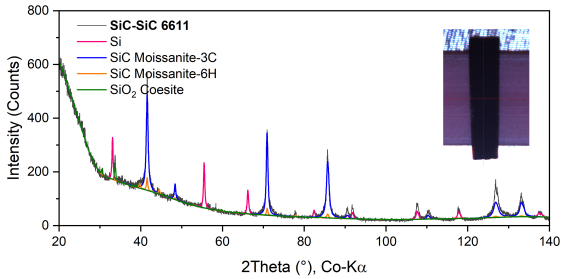

Figure 12. XRD of SiC-CTP in the as-received state.

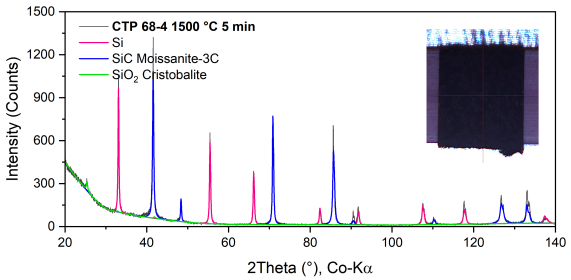

Figure 13. XRD of SiC-CTP after high-temperature oxidation at 1 550 °C for 5 min.

This transformation reflected the instability of coesite under oxidizing high-temperature conditions. The persistence of Si and SiC peaks suggested that oxidation primarily affected the near-surface region.

The microstructure of the FeCrAl alloy after high-temperature oxidation tests was investigated by transmission Mössbauer spectroscopy (TMS) and CEMS, which allowed us to focus on the local environment of ^{57}Fe. Figure 14 shows the RT CEMS spectrum of a FeCrAl sample exposed to 1 350 °C for 180 min. The spectrum displayed a relatively broad six-line pattern, which was fitted using a distribution of hyperfine magnetic fields. The distribution reached a maximum around 30 T and gradually decreased toward lower fields, resulting in a mean hyperfine field of approximately 26 T. The corresponding average isomer shift was about 0.01 mm s^{-1}. These features are consistent with the presence of the α-Fe or α'-Fe phase, where the local environment of Fe atoms is modified by substitutional Cr and Al atoms in the nearest coordination shells, leading to a modification of the hyperfine magnetic field. No spectral features indicating the presence of iron oxides were detected,

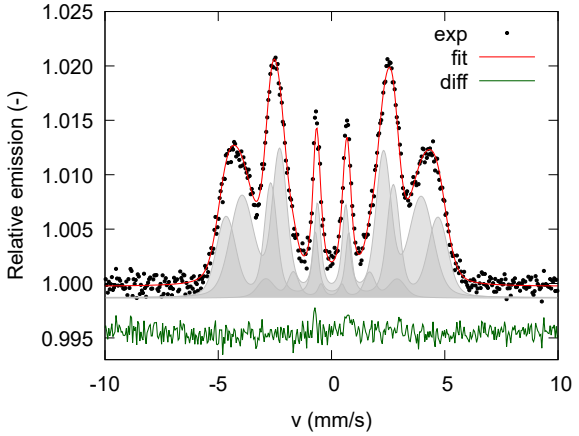

FIGURE 14. CEMS spectrum of the FeCrAl sample exposed to 1 350 °C for 180 min recorded at RT.

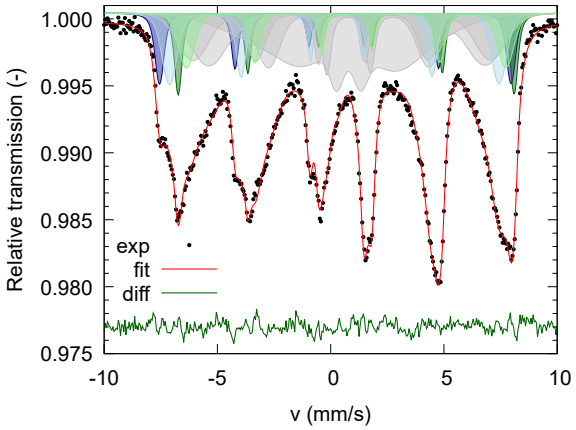

FIGURE 15. TMS spectrum of the FeCrAl sample fragment exposed to 1 375 °C for 30 min recorded at RT.

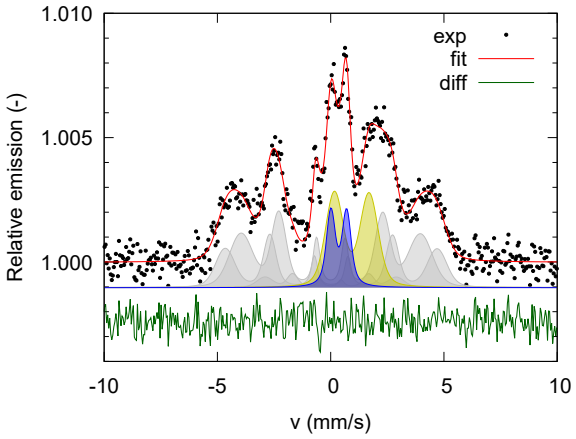

FIGURE 16. CEMS spectrum of the FeCrAl sample fragment exposed to 1 375 °C for 6.5 min (RAMP test) recorded at RT.

suggesting that the near-surface region probed by CEMS remained free of significant oxide formation under the applied conditions.

The TMS spectrum of an alloy fragment from a FeCrAl sample annealed at 1 375 °C for 30 min is presented in Figure 15. The spectrum exhibited an asymmetric sextet extending to higher velocity values, indicating the presence of components with larger hyperfine magnetic fields. Two relatively sharp sextets, shown in blue ($IS = 0.24 \pm 0.02\,\mathrm{mm\,s^{-1}}$, $QS = -0.07 \pm 0.04\,\mathrm{mm\,s^{-1}}$, $B_{\mathrm{hf}} = 48.2 \pm 0.5\,\mathrm{T}$) and green ($IS = 0.66 \pm 0.02\,\mathrm{mm\,s^{-1}}$, $QS = 0.05 \pm 0.04\,\mathrm{mm\,s^{-1}}$, $B_{\mathrm{hf}} = 46.0 \pm 0.5\,\mathrm{T}$), are likely associated with non-stoichiometric Fe_3O_4 phases [13]. In addition, two broader six-line components – depicted in light-blue and light-green – exhibited slightly lower hyperfine fields and may correspond to more disordered regions within the Fe_3O_4 structure. The broad underlying contribution, shown in gray, may originate from very small iron oxide nanoparticles undergoing superparamagnetic relaxation at room temperature, or from structurally disordered iron oxide phases. It should be noted, however, that a precise identification of individual iron oxide phases in such a complex and overlapping spectrum is inherently challenging and often non-unique without complementary characterization techniques.

The CEMS spectrum of the FeCrAl sample subjected to a rapid thermal annealing (RAMP) procedure at 1 375 °C is shown in Figure 16. Similar to the FeCrAl sample exposed to 1 350 °C for 180 min, the spectrum exhibited a broad magnetic sextet consistent with the α-Fe or α'-Fe phase. In addition to this magnetic component, the spectrum also revealed two paramagnetic doublets. The first, depicted in blue, was characterized by hyperfine parameters $IS = 0.36 \pm 0.02\,\mathrm{mm\,s^{-1}}$ and $QS = 0.70 \pm 0.04\,\mathrm{mm\,s^{-1}}$. According to Cotica et al. [14], this doublet may be attributed to Fe^{3+} in an "iron-poor" solid solution of α-$(FeAl)_2O_3$. Very similar hyperfine parameters were also reported by Waanders et al. [15] for $FeCr_2O_4$ ($IS = 0.28\,\mathrm{mm\,s^{-1}}$, $QS = 0.64\,\mathrm{mm\,s^{-1}}$), suggesting that this signal might originate from mixed Cr–Al iron oxides formed during oxidation. The second doublet, shown in yellow, was significantly broader and exhibited hyperfine parameters of $IS = 0.93 \pm 0.02\,\mathrm{mm\,s^{-1}}$ and $QS = 1.53 \pm 0.04\,\mathrm{mm\,s^{-1}}$. The large linewidth suggests a poorly ordered phase rather than a well-crystallized compound. The relatively high isomer shift and quadrupole splitting are indicative of Fe^{2+}, and the parameters closely match those reported for hercynite ($FeAl_2O_4$) by Cotica and Paesano [14, 16]. The presence of both Fe^{2+} and Fe^{3+} species in the near-surface region indicates partial oxidation and spinel-related phase formation during the short but intense thermal treatment. Given the complexity and overlap of the spectral features, unambiguous phase identification remains challenging and may benefit from complementary techniques.

3.3. RCT AND MICROHARDNESS

Tables 4 and 5 summarize the RCT results. All SiC-CTP samples were very brittle, with offset strain

Temp. during RCT [°C]	Temp. [°C] / exposure time [min]	Offset strain [%]	Max. load [N]
20*	–	0.12	144
135*	–	0.70	3
135	1 200/60	0.08	3
135	1 200/30	0.31	38
135	1 200/30	0.47	64
20	1 200/60	0.34	94
20	1 200/30	0.19	135
20	1 350/30	0.68	6
20	1 500/5	0.04	16
20	1 300/30	0.30	6
20	1 400/15	0.06	48
20	1 400/30	0.04	27
20	1 400/60	0.87	27
20	1 450/1	0.32	24

* as-received state

Table 4. Results of RCT test for SiC-CTP samples – Offset strain and maximal load.

Temp. during RCT [°C]	Temp. [°C] / exposure time [min]	Offset strain [%]	Max. load [N]
135	1 300/30	22.46	68
135	1 300/180	22.47	94
135	1 300/90	22.38	75
135	1 350/90	22.93	56
135	1 350/180	23.19	86

Table 5. Results of RCT test for FeCrAl samples – Offset strain and maximal load.

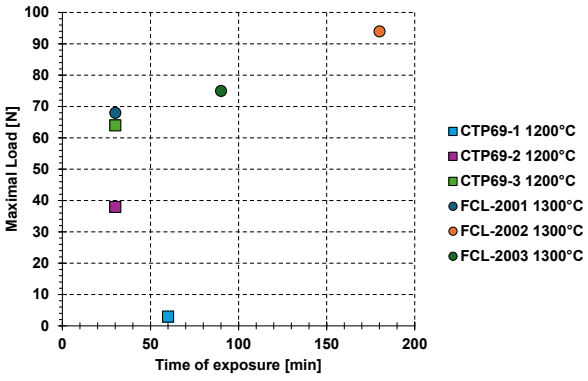

Figure 17. Offset strain as a function of exposure time for selected SiC-CTP and FeCrAl (FCL) samples.

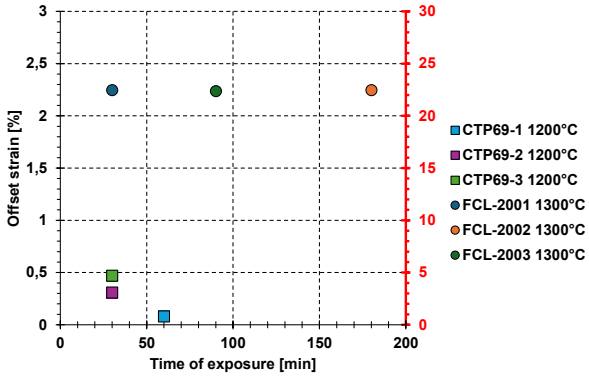

Figure 18. Maximum load as a function of exposure time for selected SiC-CTP and FeCrAl (FCL) samples (red axis).

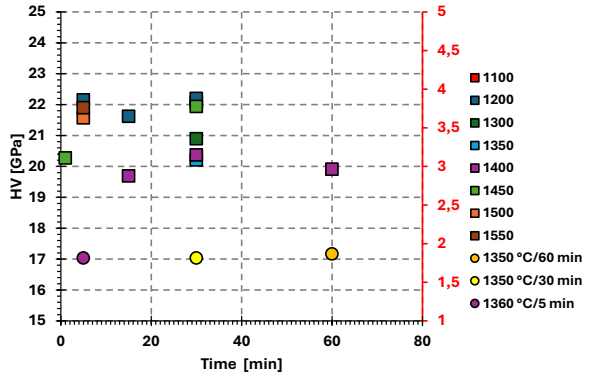

Figure 19. Average microhardness of SiC-CTP (HV1, squares) compared to FeCrAl (HV0.1, circles, red axis) after high-temperature oxidation.

far below the 1 % permanent strain criterion used for zirconium alloys [17]. By contrast, FeCrAl maintained offset strain above 20 % even after exposure at 1 300 °C. Representative trends are shown in Figures 17 and 18.

Microhardness measurements of the inner CVD layer of SiC-CTP (Figure 19) remained consistently high (19 GPa to 23 GPa) with no significant dependence on temperature, indicating microstructural stability. FeCrAl hardness was much lower (∼2 GPa), with slight increases after prolonged exposure attributed to the formation of surface alumina rather than bulk changes.

4. Discussion

High-temperature oxidation experiments were carried out on SiC samples in the temperature range of 1 100 °C–1 550 °C and on FeCrAl alloy samples from 1 300 °C to 1 375 °C. The results demonstrated the superior oxidation resistance of SiC-CTP, as the weight gain remained minimal even at the highest test temperatures. In contrast, FeCrAl samples exhibited significantly higher mass changes above 1 350 °C. Some samples even showed negative weight gain, indicating oxide spallation or volatilization. These observations suggest that once a critical temperature was exceeded, oxidation kinetics were dominated by the breakdown of the protective alumina layer.

Figure 10d shows the RAMP test, in which the sample was gradually heated from 900 °C to 1 375 °C over a total of 6.5 minutes. This provided sufficient time for the formation of a continuous Al_2O_3 layer. The protective oxide prevented rapid oxidation and disintegration. However, above approximately 1 375 °C,

this protective behavior was no longer observed. Instead of alumina, iron-rich spinel oxides with much faster growth kinetics were formed, offering insufficient protection and leading to rapid degradation. These results highlight the importance of heating rate and oxide formation kinetics in determining the stability of FeCrAl alloys under accident-like scenarios.

Microstructural analysis supported these trends. In SiC, SEM and XRD revealed the formation of a SiO_2 surface layer, which likely acted as a diffusion barrier and contributed to the observed stability. In FeCrAl, distinct phases of both aluminum and iron oxides were detected. Their evolution with increasing temperature was consistent with the loss of protective behavior at high temperatures. Mössbauer spectroscopy, including both TMS and CEMS, further revealed the presence of magnetic α-Fe phases and complex iron oxide species in the near-surface regions, providing deeper insight into the oxidation mechanisms.

Mechanical testing highlighted the contrasting behavior of the two materials. FeCrAl maintained a post-exposure offset strain above 20 % even after oxidation at 1 300 °C, suggesting that the alloy retained good mechanical integrity under these conditions. By contrast, SiC remained brittle, with values well below 1 %, limiting its tolerance to mechanical stress despite its excellent thermal and oxidation resistance. This trade-off underscores the key challenge of SiC: although thermally robust, its brittleness restricts its practical application as cladding without additional engineering solutions.

Overall, these findings emphasize that both materials have complementary strengths and limitations. SiC offers outstanding thermal and chemical stability but suffers from intrinsic brittleness, while FeCrAl provides mechanical robustness yet loses oxidation resistance above a critical temperature. A deeper understanding of these mechanisms is essential for designing next-generation ATF cladding systems.

5. Conclusion

This study compared the high-temperature oxidation behavior of SiC-CTP composites and FeCrAl alloys as candidate ATF cladding materials.

SiC-CTP exhibited excellent thermal resistance, withstanding exposure up to 1 550 °C with only minimal mass change. The formation of a protective SiO_2 surface layer contributed to its stability. However, its intrinsic brittleness, with offset strain values well below 1 %, remains a major drawback for practical applications.

FeCrAl retained its mechanical integrity up to 1 350 °C, maintaining offset strain above 20 %. Its protective behavior was linked to the formation of a continuous Al_2O_3 layer, particularly under slow heating conditions. At higher temperatures, however, this protection was lost due to the rapid growth of iron-rich spinel oxides, leading to accelerated degradation.

In conclusion, SiC offers superior oxidation resistance but limited mechanical tolerance, while FeCrAl provides mechanical robustness with reduced high-temperature stability. These complementary strengths underline the importance of tailoring protective oxide formation and combining materials knowledge with engineering design to optimize ATF cladding performance in severe accident scenarios.

Acknowledgements

This work was supported by the TACR project No. TN02000012 and by Large Research Infrastructures of the Ministry of Education, Youth and Sports of the Czech Republic: LM2023073. The authors gratefully acknowledge the provision of experimental materials and valuable technical support from the Karlsruhe Institute of Technology (KIT) and Ceramic Tubular Products, LLC (CTP). Their contribution was essential to the successful execution of the high-temperature oxidation experiments. The authors also thank all collaborating researchers and laboratory staff involved in the material preparation, testing, and analysis phases of this study.

References

[1] B. A. Pint, K. A. Terrani, Y. Yamamoto, L. L. Snead. Material selection for accident tolerant fuel cladding. *Metallurgical and Materials Transactions E* **2**:190–196, 2015. https://doi.org/10.1007/s40553-015-0056-7

[2] K. A. Terrani. Accident tolerant fuel cladding development: Promise, status, and challenges. *Journal of Nuclear Materials* **501**:13–30, 2018. https://doi.org/10.1016/j.jnucmat.2017.12.043

[3] Z. Li, X. Zhang, Q. Zhang, et al. Oxidation and mechanical properties of SiC fibers after high temperature exposure in air and steam. *Journal of the European Ceramic Society* **44**:6864–6874, 2024. https://doi.org/10.1016/j.jeurceramsoc.2024.04.076

[4] M. Steinbrück, M. Große, U. Stegmaier, et al. High-temperature oxidation of silicon carbide composites for nuclear applications. In *Proceedings of the TOPFUEL 2021 Conference*. 2021. https://doi.org/10.5445/IR/1000141512

[5] M. Herrmann, P. Meisel, W. Lippmann, A. Hurtado. Joining technology – A challenge for the use of SiC components in HTRs. *Nuclear Engineering and Design* **306**:170–176, 2016. https://doi.org/10.1016/j.nucengdes.2015.12.022

[6] W.-J. Kim, D. Kim, J. Y. Park. Fabrication and material issues for the application of SiC composites to LWR fuel cladding. *Nuclear Engineering and Technology* **45**(4):565–572, 2013. https://doi.org/10.5516/NET.07.2012.084

[7] W. A. Curtin. Theory of mechanical properties of ceramic-matrix composites. *Journal of the American Ceramic Society* **74**(11):2837–2845, 1991. https://doi.org/10.1111/j.1151-2916.1991.tb06852.x

[8] S. Dryepondt, K. A. Unocic, D. T. Hoelzer, et al. Development of low-Cr ODS FeCrAl alloys for accident-tolerant fuel cladding. *Journal of Nuclear Materials* **501**:59–71, 2018. https://doi.org/10.1016/j.jnucmat.2017.12.035

[9] K. G. Field, X. Hu, K. C. Littrell, et al. Radiation tolerance of neutron-irradiated model Fe-Cr-Al alloys. *Journal of Nuclear Materials* **465**:746–755, 2015. https://doi.org/10.1016/j.jnucmat.2015.06.023

[10] C. Kim, C. Tang, M. Grosse, et al. Oxidation mechanism and kinetics of nuclear-grade FeCrAl alloys in the temperature range of 500–1500 °C in steam. *Journal of Nuclear Materials* **564**:153696, 2022. https://doi.org/10.1016/j.jnucmat.2022.153696

[11] Z. Sun, Y. Yamamoto. Processability evaluation of a Mo-containing FeCrAl alloy for seamless thin-wall tube fabrication. *Materials Science and Engineering: A* **700**:554–561, 2017. https://doi.org/10.1016/j.msea.2017.06.036

[12] T. Žák, Y. Jirásková. CONFIT: Mössbauer spectra fitting program. *Surface and Interface Analysis* **38**(4):710–714, 2006. https://doi.org/10.1002/sia.2285

[13] J. Winsett, A. Moilanen, K. Paudel, et al. Quantitative determination of magnetite and maghemite in iron oxide nanoparticles using Mössbauer spectroscopy. *SN Applied Sciences* **1**:1636, 2019. https://doi.org/10.1007/s42452-019-1699-2

[14] L. F. Cótica, S. C. Zanatta, S. N. de Medeiros, et al. Mechanical milling of the $(\alpha\text{-}Fe_2O_3)_x(\alpha\text{-}Al_2O_3)_{1-x}$ system: An X-ray diffraction and Mössbauer spectral study. *Solid State Ionics* **171**(3-4):283–288, 2004. https://doi.org/10.1016/j.ssi.2004.04.018

[15] F. B. Waanders, S. W. Vorster, A. Engelbrecht. Mössbauer and SEM characterisation of the scale on type 304 stainless steel. *Scripta Materialia* **42**(10):997–1000, 2000. https://doi.org/10.1016/S1359-6462(00)00322-5

[16] A. Paesano Jr., C. K. Matsuda, J. B. M. da Cunha, et al. Synthesis and characterization of Fe-Al_2O_3 composites. *Journal of Magnetism and Magnetic Materials* **264**(2-3):264–274, 2003. https://doi.org/10.1016/S0304-8853(03)00215-4

[17] Draft regulatory guide DG-1262 testing for post quench ductility, 2014.